Acta Geologica Sinica (English Edition), 2019, 93(4): 810–819

A Quantitative Method for Active Fault Migration Distance Assessment on both Sides of Mid-Ocean Ridges—Based on Multi-Beam Data

FAN Qingkai[1, 2], LI Jianghai[1, 2, *], LIU Zhonglan[1, 3] and LIU Chiheng[1, 2, 4]

[1] *Key Laboratory of Orogenic Belts and Crustal Evolution, Ministry of Education, School of Earth and Space Sciences, Peking University, Beijing 100871, China*
[2] *Institute of Oil and Gas, Peking University, Beijing 100871, China*
[3] *MARUM, Center for Marine Environmental Sciences, University of Bremen, 28334, Germany*
[4] *Division of Geology and Mineral Resources, Beijing Research Institute of Uranium Geology. Beijing 100029, China*

Abstract: Fracture-fissure systems found at mid-ocean ridges are dominating conduits for the circulation of metallogenic fluid. Ascertaining the distribution area of active faults on both sides of mid-ocean ridges will provide a useful tool in the search for potential hydrothermal vents, thus guiding the exploration of modern seafloor sulfides. Considering the Mid-Atlantic Ridge 20°N–24°N (NMAR) and North Chile Rise (NCR) as examples, fault elements such as Fault Spacing (ΔS) and Fault Heave (ΔX) can be identified and quantitatively measured. The methods used include Fourier filtering of the multi-beam bathymetry data, in combination with measurements of the topographic slope, curvature, and slope aspect patterns. According to the Sequential Faulting Model of mid-ocean ridges, the maximal migration distance of an active fault on either side of mid-ocean ridges—that is, the distribution range of active faults—can be measured. Results show that the maximal migration distance of active faults at the NMAR is 0.76–1.01 km (the distance is larger at the center than at the ends of this segment), and at the NCR, the distribution range of active faults is 0.38–1.6 km. The migration distance of active faults on the two study areas is positively related to the axial variation of magma supply. In the NCR study area, where there is an abundant magma input, the number of faults within a certain distance is mainly affected by the variation of lithospheric thickness. Here a large range of faulting clearly corresponds to a high proportion of magmatism to seafloor spreading near mid-ocean ridges (M) value, and in the study area of the NMAR, there is insufficient magmatism, and the number of faults may be controlled by both lithospheric thickness and magma supply, leading to a less obvious positive correlation between the distribution range of active faults and M.

Key words: migration distance of active faults, quantitative assessment, Mid-Atlantic Ridge, North Chile Rise, multi-beam bathymetry

Citation: Fan et al., 2019. A Quantitative Method for Active Fault Migration Distance Assessment on both Sides of Mid-Ocean Ridges—Based on Multi-Beam Data. Acta Geologica Sinica (English Edition), 93(4): 810–819. DOI: 10.1111/1755-6724.13850

1 Introduction

The discovery of submarine hydrothermal vents at the Galápagos Rift in 1977 (Corliss et al., 1979) began a period of intensive global seafloor exploration that continues today. More than 150 hydrothermal venting sites and massive seafloor sulfide deposits have been found on mid-ocean ridges. This includes the East Pacific Rise (EPR), the Mid-Atlantic Ridge (Rona et al., 1986; Langmuir et al., 1997; German and Parson, 1998), and the Southwest Indian Ridge (SWIR, Tao et al., 2011, 2012; Chen et al., 2018; Liu et al., 2018). As the main circulation channels of the hydrothermal fluids (Franklin et al., 1981; Herzig and Hannington., 1995), fracture-fissure system of mid-ocean ridges are the crucial factor controlling the formation of modern seafloor hydrothermal sulfides and ore deposits. Most seafloor hydrothermal activities near mid-ocean ridges are assumed to focus around axial median valley margins where faults are active. On-site observations confirm this (Kappel and Franklin, 1989; Karson and Rona, 1990; Herzig and Hannington., 1995). Therefore, ascertaining the distribution range of active faults may help in narrowing the potential distribution range of hydrothermal activities, providing a focus for seafloor hydrothermal exploration localities.

Faulting on both sides of mid-ocean ridges is affected by factors such as magma supply rate, distance from the axis, and lithospheric thickness (Forsyth, 1992; Buck, 1993; Buck et al., 2005; Behn and Ito, 2008). Continuous faulting not only brings about the off-axis displacement of faults but also bends the footwall (Lavier et al., 2000; Olive and Behn, 2014), producing the stripped topographic relief that runs parallel to the ridge axis. Slow-spreading ridges develop axial valleys, with fault scarp throws greater than 200 m. Fast-spreading ridges develop axial high topography, with smaller faults whose throws

* Corresponding author. E-mail: jhli@pku.edu.cn

are usually less than 50 m. Intermediate-spreading ridges are transitioning between fast- and slow-spreading centers, represented by the alternation of axial valleys and axial highs (MacDonald, 1982; Goff et al., 1995; Small, 1994, 1998; Smith, 2013).

Previous studies mainly focused on faulting mechanisms near mid-ocean ridges (Forsyth, 1992; Buck, 1993; Lavier et al., 2000; Buck et al., 2005; Behn and Ito, 2008). So far, no specific study on the distribution pattern of active faults on mid-ocean ridges as measured with multi-beam bathymetry has been performed and published. Mid-Atlantic Ridge 20°N–24°N and North Chile Rise (NCR) were selected as testing areas. Fault locations were identified, and fault elements were measured through Fourier filtering on the multi-beam bathymetry. The distribution range of active faults was quantitatively assessed based on the kinematic Sequential Faulting Model.

2 Method for Assessing the Faulting Range

2.1 Data sources

Mid-Atlantic Ridge 20°N–24°N (NMAR) and North Chile Rise (NCR) were selected as study locations where the distribution range of active faults on both sides of mid-ocean ridges could be assessed. Fast-spreading ridges (e.g., EPR) often develop small faults, which are difficult or impossible to recognize on the limited resolution available through multi-beam bathymetry. Owing to the chaotic pattern of faults, ultraslow-spreading ridges (e.g., SWIR) are also not ideal places to calculate the faulting range. Therefore, slow- and intermediate-spreading ridges were purposefully selected as testing areas.

Study areas, as viewed through bathymetry data, can be characterized as follows: 1) uniform spreading rate (NMAR, the full spreading rate is 50.5–51 mm/year; NCR, ~62 mm/year), 2) spreading direction orthogonal to the mid-ocean ridge axis, 3) regular distribution pattern of faults on both sides of the ridge axis, which has been thoroughly studied by previous studies (NMAR: Shaw and Lin, 1993; Escartín et al., 1999; NCR: Tebbens et al., 1997; Howell et al., 2016), and 4) bathymetry data is open, having high accuracy (Ryan et al., 2009), and suitable for the identification and measurement of fault elements and quantitative evaluation of the distribution range of active faults.

The multi-beam bathymetry data of the NMAR and NCR were from the Marine Geoscience Data System (http://www.marine-geo.org/portals/gmrt/, Ryan et al., 2009). The measurements of the fault elements in the NCR were derived from the topographic interpretation of Howell et al. (2016).

2.2 Quantitative measurement of fault elements

The topographic relief data collected on both sides of mid-ocean ridges are mainly composed of large- and small -wavelength signals. The large-wavelength relief, caused by off-axial variations of the magma supply and the cooling effect of new-forming oceanic crust, has an adverse effect on fault identification and should be eliminated. In order to do this, two kinds of signals need to be separated (Olive et al., 2015; Howell et al., 2016; Liu and Buck, 2018), and just the fault elements needed were quantitatively measured on the filtered small-wavelength bathymetry map.

Taking the NMAR 20°N–24°N segment as an example (Fig. 1), a Fourier high-pass filter, applied using a Matlab script, is used to decompose the primary bathymetry (Figs. 1a, 1d). After many attempts (Howell et al., 2016; Liu and Buck, 2018), 20 km was chosen as the threshold to filter the large-scale relief-related (wavelength >20 km) effects on fault element recognition (Figs. 1b, 1e) and to preserve and highlight the small-scale topographic relief caused by faulting (wavelength <20 km; Figs. 1c, 1f) so that quantitative interpretations can be produced.

According to the off-axis micro-seismic results on NMAR (Wolfe et al., 1995), faulting near mid-ocean ridges is constrained within 10 km off-axis on either side. McAllister and Cann (1996) defined the distance between the mid-ocean ridge axis and the farthest faulting away as the “fault growth window,” which is 10 km here. Calculation of the distribution of active faults mainly refers to stable, inactive faults to avoid the effect of these active faults within the “fault growth window” on the result. The identification and measurement of fault elements were only implemented outside the “window.”

In the study area of NMAR 20°N–24°N, the bathymetry map with a wavelength less than 20 km was chosen, and 12 topographic profiles were selected (Fig. 6a), each with equal length and nearly equidistant from each other. By combining the distribution law that the top and bottom of a fault scarp correspond to “low slope and high curvature” with the distribution pattern of the slope aspect (Fig. 2), the top and bottom of fault scarps outside the “fault growth window” were identified (Fig. 3), and Fault Spacing (ΔS) and Fault Heave (ΔX) in each profile were measured. These results provide basic data (Table 1) for the calculation of the distribution range of active faults.

2.3 Calculation of the faulting range

Previous numerical simulations (Buck, 2005; Behn and Ito, 2008) showed that new faults near mid-ocean ridges generally develop dipping toward the axis and mostly form on the opposite side of pre-existing inactive faults (Fig. 4). The Sequential Faulting Model (Shaw and Lin, 1993; Buck et al., 2005; Behn and Ito, 2008) refers to the sequential growth of faults on both sides of mid-ocean

Table 1 Interpretation of topographic profiles from Mid–Atlantic Ridge 20˚ N–24˚ N

Profile number	Profile location (Center)	Fault Amount		Average fault spacing (km)	Average fault heave (km)
		West half	East half		
1	23°20′N	21	23	3.69	1.76
2	23°10′N	26	24	3.19	1.58
3	23°00′N	27	22	3.36	1.66
4	22°48′N	30	26	2.90	1.38
5	22°40′N	25	22	3.39	1.59
6	22°30′N	27	26	2.92	1.33
7	22°24′N	26	26	3.10	1.45
8	22°10′N	21	22	3.73	1.82
9	22°04′N	23	27	3.20	1.47
10	21°57′N	24	21	3.55	1.77
11	21°45′N	22	20	3.65	1.59
12	21°26′N	23	19	3.79	1.77

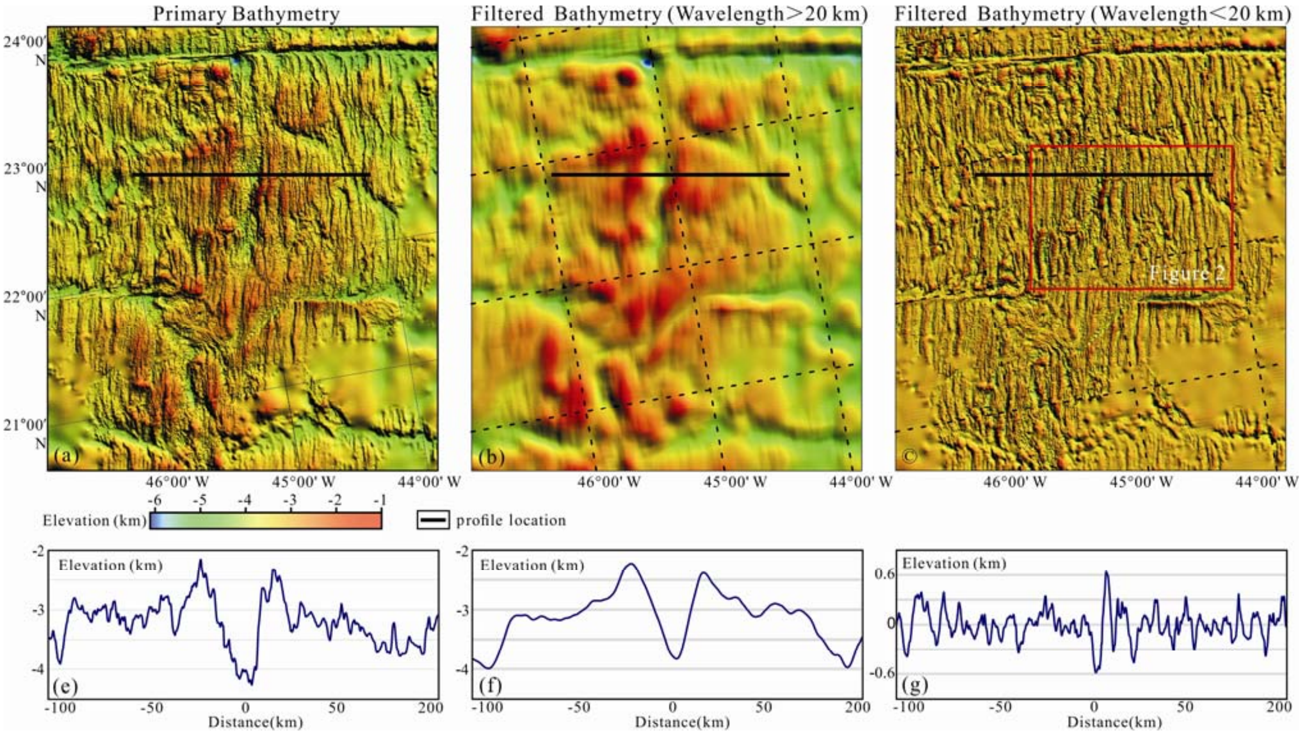

Fig. 1. Bathymetry before and after filtering at North Mid-Atlantic Ridge 20°N–24°N.
(a) Original bathymetry; (b) bathymetry after filtering (wavelength > 20 km); (c) bathymetry after filtering (wavelength < 20 km); (d), (e) and (f) topographic profiles corresponding to black lines in a, b and c, respectively.

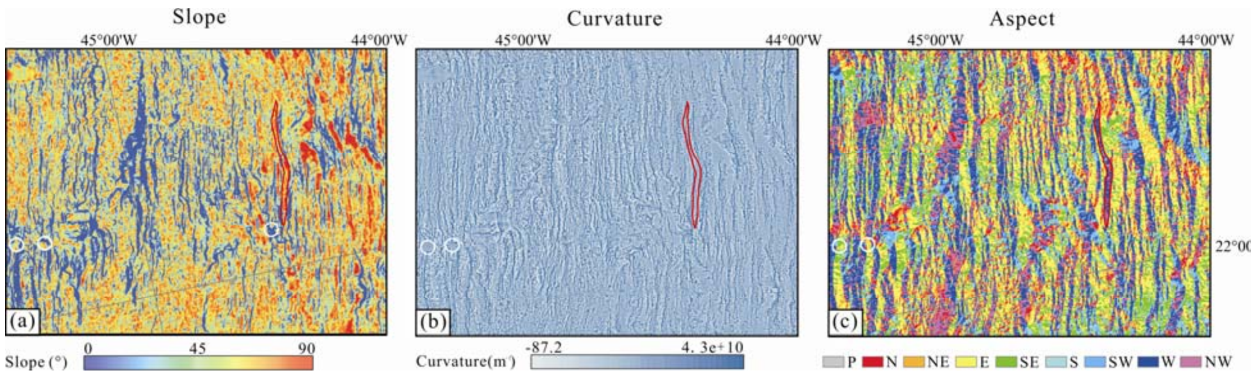

Fig. 2. The distribution of slope, curvature and aspect (location shown in Fig. 1c).
Red ribbons and white circles represent fault planes and volcanic mounds respectively.

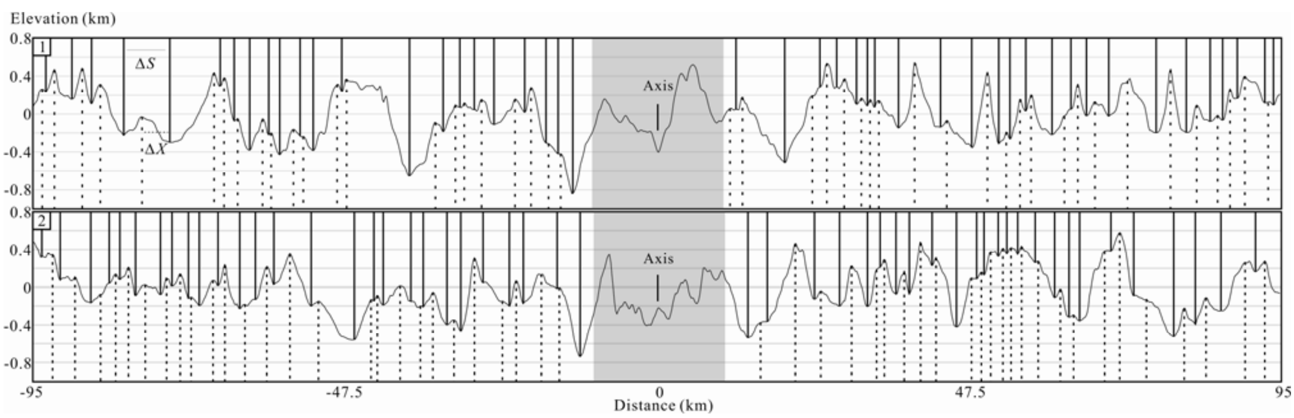

Fig. 3. Example sections of Mid-Atlantic Ridge 20°N–24°N and identifications of fault scarps' top and bottom.
Location of these sections are shown in Fig.6a, the solid and dashed lines indicate the scarp bottoms and tops, respectively. Gray areas denote 'fault growth window' ('fault growth window' is from Wolfe et al., 1995; Escartin et al., 1999).

ridges where there is only one active fault near a ridge axis at any time, and the tectonic strain is focused mainly on these active faults.

In this model, at one side near the mid-ocean ridge, an active fault developed, and then, both new active faults and inactive faults migrated off-axially as a result of seafloor spreading. As the distance from the axis increases, the lithosphere thickness increases, and the stress accumulation of the lithosphere proximal to the fault gradually increases. The friction (F_F, *Eq.*1, Olive et al., 2015) required to sustain faulting also increases gradually (Forsyth, 1992; Buck, 1993). Continuous faulting activity not only brings about off-axis displacement of new-forming crust but also bends fault footwalls, producing an accumulation of stress (F_B, *Eq.*2, Lavier et al., 2000). When the stress produced by the off-axial displacement (F_F + F_B) exceeds the required stress to develop a new fault (F_I, *Eq.*3, Olive et al., 2015), a new active fault is created at the other side of the axis, and the pre-existing active fault becomes inactive.

$$F_F = \frac{\mu\rho_m gH^2(\Delta X)}{2\mu\sin^2\left(\theta(\Delta X)\right)+\sin\left(\theta(\Delta X)\right)\cos\left(\theta(\Delta X)\right)} \quad (1)$$

$$F_B = AH^2(\Delta X)\left(1-e^{-B\Delta X/H(\Delta X)}\right) \quad (2)$$

$$F_I = \frac{\mu\rho_m gH^2/2+HC}{\mu\sin^2\theta+\sin\theta\cos\theta} \quad (3)$$

A and *B* for the proofreading numerical model constants are 5000 Pa/m and 50, respectively (Behn and Ito, 2008; Olive et al., 2015), μ is the coefficient of friction, ρ is the lithosphere density, *G* is the gravitational acceleration, *H* is the thickness of the lithosphere, ΔX is the Fault Heave, and θ is the dipping angle of a new fault.

Sequential fault growth near the ridge axis leads to asymmetric off-axis displacement of faults on both sides of the ridge (Buck et al., 2005). Assuming the half spreading rate is μ_s and the proportion of magmatism to the seafloor spreading near mid-ocean ridges is *M* (Fig. 4), then the tectonic extension rate is represented by $2u_s$ (1−M). Because tectonic extension always accumulates around the fault nearest the ridge axis, the active fault migrates off-axially at a rate of $\mu_{AF} = 2\mu_s$ (M−0.5), and the inactive one on the opposite side migrates at a rate of $\mu_{IF} = \mu_s$.

The asymmetric off-axis migration of faults from both sides of mid-ocean ridges indicates that Fault Heave (ΔX, Fig. 4) and Fault Spacing (ΔS, Fig. 4) are two functions (*Eq.*4 and *Eq.*5) of *M* and the maximum off-axis migration distance of active faults, X_{AF} (Behn and Ito, 2008):

$$\Delta X = \frac{1-M}{M-0.5}X_{AF} \quad (4)$$

$$\Delta S = \frac{M}{M-0.5}X_{AF} \quad (5)$$

*Eq.*4 and *Eq.*5 (Buck et al., 2005; Behn and Ito, 2008) can be derived into

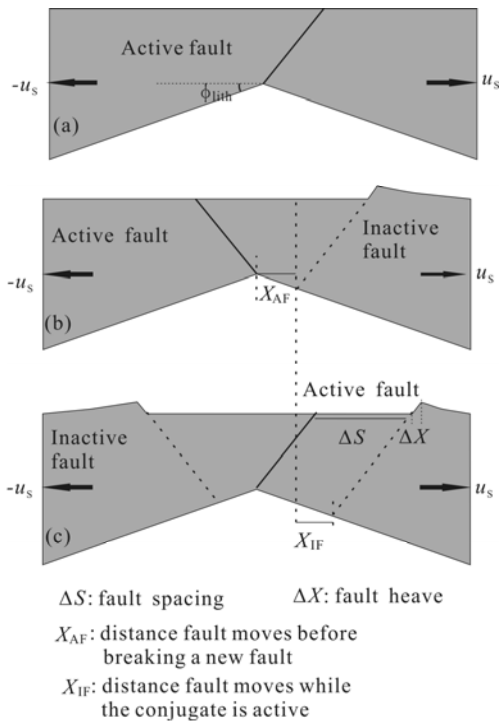

Fig. 4. Sequential Faulting Model of mid-ocean ridges (Buck et al., 2005; Behn and Ito, 2008).

$$M = \frac{2X_{AF}+\Delta X}{2\left(\Delta S - X_{AF}\right)} \quad (6)$$

$$M = \frac{\Delta S}{2\left(\Delta S - X_{AF}\right)} \quad (7)$$

Combining *Eq.*6 and *Eq.*7, the maximum off-axis migration distance of active faults can be obtained, X_{AF}:

$$X_{AF} = \frac{\Delta S-\Delta X}{2} \quad (8)$$

In this study, *Eq.*8 is used to calculate the maximum off -axis migration distance of active faults on both sides of mid-ocean ridges—the “faulting range.” It should be noted that the X_{AF} refers to the distance between the beginning and cessation of active faults on the same side of the mid-ocean ridge rather than the true off-axis distance. In general, intermediate- and slow-spreading ridges develop different forms of median rift valley bounded by normal faults (MacDonald, 1982), and there is no large-scale fault in the valley. It is thus supposed that faulting on both sides of mid-ocean ridges begin at the edge of the median rift valley, and X_{AF} is the distance between the edge of the median rift and the position where faulting ceases. The region between that position and the ridge axis can be regarded as a potential zone for hydrothermal venting too.

3 Migration Distance of Active Faults of NMAR and NCR Testing Zones

3.1 North Mid-Atlantic Ridge 20°N–24°N

The NMAR 20°N–24°N segment (Fig. 5a) is a slow-spreading ridge, developing a 20–30 km wide, 1–3 km deep median rift valley at axis (Figs. 5b, 5c). The topographic profiles orthogonal to the ridge axis have an axial cross correlation coefficient variation similar to the typical slow-spreading ridge (Fig. 5d, Stoddard and Jurdy, 2012). On both sides of this ridge, the topographic slope aspects are mainly NW and SE (Fig. 5e), and the topographic relief is parallel to the ridge axis. Tectonically, the NMAR study area is located north of the first-order segment bounded by the Kane Transform Fault and 15°20’ N Transform Fault. The topographic profiles selected are all located on the second-order segment south of Kane Transform Fault and north of 21°20’ N Fault (Fig. 6a, Maia and Gente, 1998).

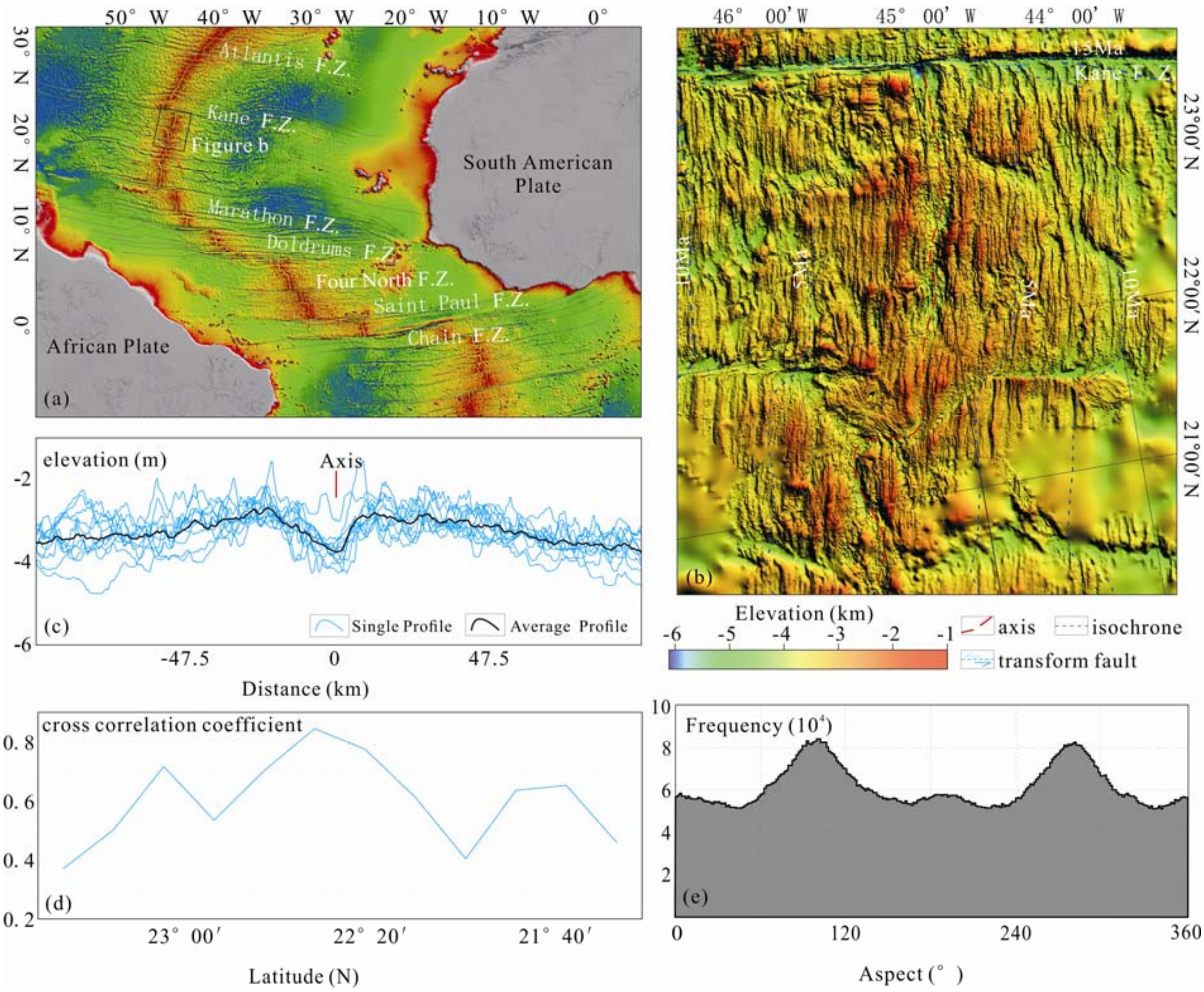

Fig. 5. Location and topographic features of Mid-Atlantic Ridge 20° N–24° N.

(a) Location of NMAR 20° N–24° N segment; (b) bathymetry of the study area; (c) individual and average cross sections (shown on Figure 6a) orthogonal to ridge axis; (d) Cross Correlation Coefficient of the profiles; (e) histogram showing the slope aspect in the study area.

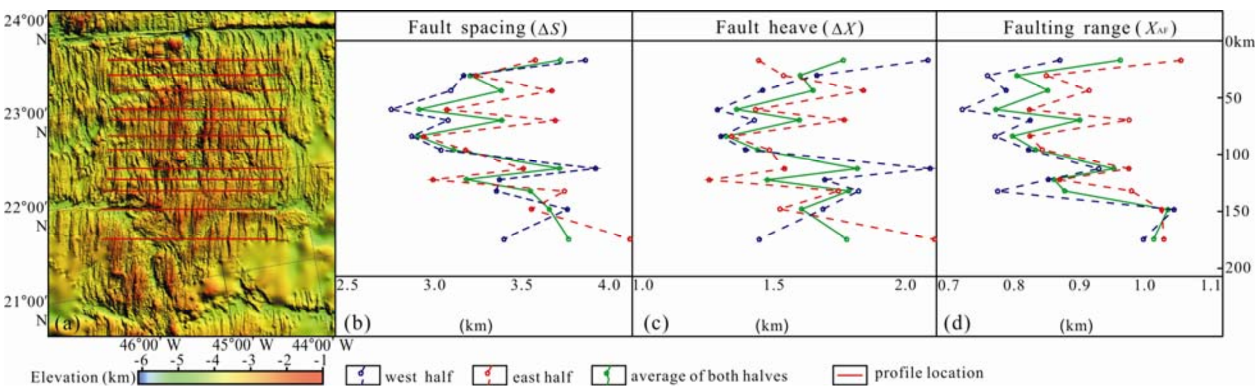

Fig. 6. Diagram showing the distribution of the fault elements and the calculation of X_{AF} values in the Mid-Atlantic Ridge 20° N –24° N

(a) Location of topographic profiles; (b) the axial variation of ΔS; (c) the axial variation of ΔX; (d) the axial variation of X_{AF}.

Measuring fault elements in study area and using the formula described above (Eq.8), the distribution area of active faults on both sides of the NMAR axis can be calculated (Fig. 6).

The maximum ΔS in the NMAR 20°N–24°N segment is 10.33 km, the minimum is less than 1.0 km, and the average value for both sides of the ridge is 2.92–3.79 km (Fig. 6b). The maximum ΔX is 9.60 km, minimum is ~0.5 km, and the average ranges from 1.33 to 1.82 km (Fig. 6c). In addition, the calculated maximum X_{AF} in this location is 3.48 km, the minimum is ~200 m, and the average ranges from 0.76 to 1.01 km (Fig. 6d). These three parameters are distributed with similar patterns, which is relatively smaller at the center of the segment than at both ends. Coincidentally, the lithospheric thickness also decreases, but the fault's size increases gradually from the center to the end of a ridge segment (Shaw and Lin, 1993; Searle and Escartín, 2004), forming detachment faults (Yu et al., 2013; Liang et al., 2014; Fan et al., 2018). The axial variations of ΔS, ΔX, and X_{AF} are consistent on both sides of the axis, but the X_{AF} of the west half is greater than that of the east (Fig. 6d), showing that the small-scale spreading rate discrepancy between the two sides of the axis in our study area (Pockalny et al., 1995; Canales et al., 2000) has some impacts on the axial range of faulting, i.e., a lower spreading rate corresponds to a larger X_{AF} value.

3.2 North Chile Rise

Chile Rise lies between the triple junction of the Pacific plate, Antarctic plate, and Nazca plate and the triple junction of the Antarctic plate, Nazca plate, and South American plate (Fig. 7, Larson et al., 1992). On the basis of the segmentation from Howell et al. (2016), the study area of the NCR is divided into 20 first-order segments (N1–N10, V1–V5, and S1–S5) and four second-order segments (N9N–N9S and S5N–S5S). According to the data volume and the regularity of topographic relief there, it was determined that seven ridge segments, such as N1, N5, and N8, were selected to calculate the maximum migration distance of active faults in the study area.

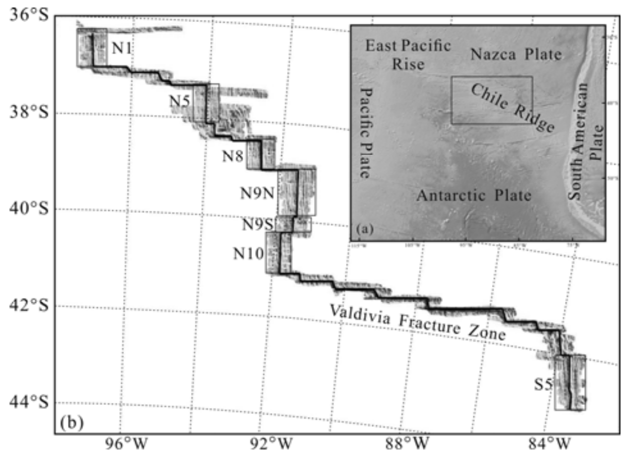

Fig. 7. Tectonic setting (a) of North Chile Rise and the segments (b) studied here

Box in Figure 7a is the location of the ridge segments selected in this paper, next to the segments are their numbers (segment number from Howell et. al., 2016).

Calculations show that (Fig. 8) the minimum X_{AF} value in the NCR study area is ~0.10 km, and the maximum is ~10.25 km. In addition, there is a certain regularity in the axial variation pattern of the average X_{AF} in the NCR. The average X_{AF} in the N1 segment gradually decreases from the center (~0.88 km) to both ends (~0.46 km). The average X_{AF} value in the N5 segment ranges from 0.74 to 1.61 km, decreasing from the south tip (~1.61 km) to the north (~0.74 km). In the N8 segment, the X_{AF} value is in the range of 0.46–1.06 km, with a "zigzag" pattern along the axis. Moreover, the range of X_{AF} in the N9N segment is between 0.59 and 0.78 km, with values in the central part that are slightly smaller than the ends. In the N9S segment, the axial variation of X_{AF} is nearly negligible, with a slightly decreasing trend from ~0.61 km at the central part to 0.53 km at the north and south. The X_{AF} value of the N10 segment has similar characteristics of axial variation as the N9N segment, increasing from ~0.49 km at the center to ~0.80 km at two ends. Finally, in the S5 segment, the range of X_{AF} values is about 0.40–0.88 km, with a decreasing trend from north to south, which is opposite from the values calculated for the N5 segment.

4 Discussion

4.1 Relationship between X_{AF} and magma supply

Comparing the axial variations of X_{AF}, ΔS, the degree of partial melting, and the M values on slow-spreading NMAR 20°N–24°N, there is a roughly positive correlation between X_{AF} and the degree of partial melting and the M values on both sides of the ridge (Fig. 9a). This kind of relationship shows that a higher degree of magma melting usually corresponds to a greater M value and a larger faulting range; by contrast, a lower degree of magma melting is related to a smaller X_{AF}. While comparing X_{AF}, ΔS, melting fraction of magma, and M values on the intermediate-spreading NCR (Howell et al., 2016), a similar but more distinct correlation between the axial variation of X_{AF} and magma supply is observed (Fig. 9b). The similar relationship between X_{AF}, M values, and the melting fraction in these two study areas indicates that the positive correlation will become more obvious as the spreading rate increases. Formation of hydrothermal vents at mid-ocean ridges is closely associated with the magmatism intensity (Franklin et al., 1981; Herzig and Hannington, 1995), which means that melting fraction grows as the spreading rate increases. Along with both of these, the faulting range also enlarges, resulting in the amplification of the potential distribution of hydrothermal activities (Hannington et al, 2011).

According to *Eq.*8, the faulting range depends on the differences in ΔS and ΔX at every single fault on both sides of mid-ocean ridges. Previous studies (Shaw and Lin, 1993; Behn and Ito, 2008) have shown that the axial variations of ΔS and ΔX have similar patterns, which increase with lithospheric thickening as the values of M approach 0.5, but the distinction between these two parameters has rarely been discussed.

In a single topographic profile, the proportion of tectonic strain in the seafloor spreading (T, ~$1 - M$) is usually expressed as the ratio of the summation of ΔX on both sides of the mid-ocean ridge in the profile to the length of the section (*Eq.*9) selected:

$$T = \frac{\sum_{i=1}^{n} \Delta X_i}{L} \tag{9}$$

ΔX_i represents the ΔX for all faults, L is the total length of the section (including the “fault growth window”), and n is the number of faults on the section. L may also be expressed in the following form (*Eq.*10):

$$L = \sum_{i=1}^{n-1} \Delta S_i \tag{10}$$

ΔS_i is the ΔS for every single fault. Therefore, the values of M can be expressed as (*Eq.*11)

$$M = \frac{\sum_{i=1}^{n-1} \Delta S_i - \sum_{i=1}^{n} \Delta X_i}{L} \approx \frac{\sum_{i=1}^{n-1}\left(\Delta S_i - \Delta X_i\right)}{L} = \frac{2X_{AF}\left(n-1\right)}{L} \tag{11}$$

*Eq.*11 shows that, in the case that the number of faults (n) is constant, X_{AF} is positively related to M values. While number of faults (n) is usually affected by M, lithospheric thickness, and magmatic cycles (Olive et al., 2015). In general, at the center of a single segment, the M value is larger, and ΔS is smaller, leading to larger n values. At the

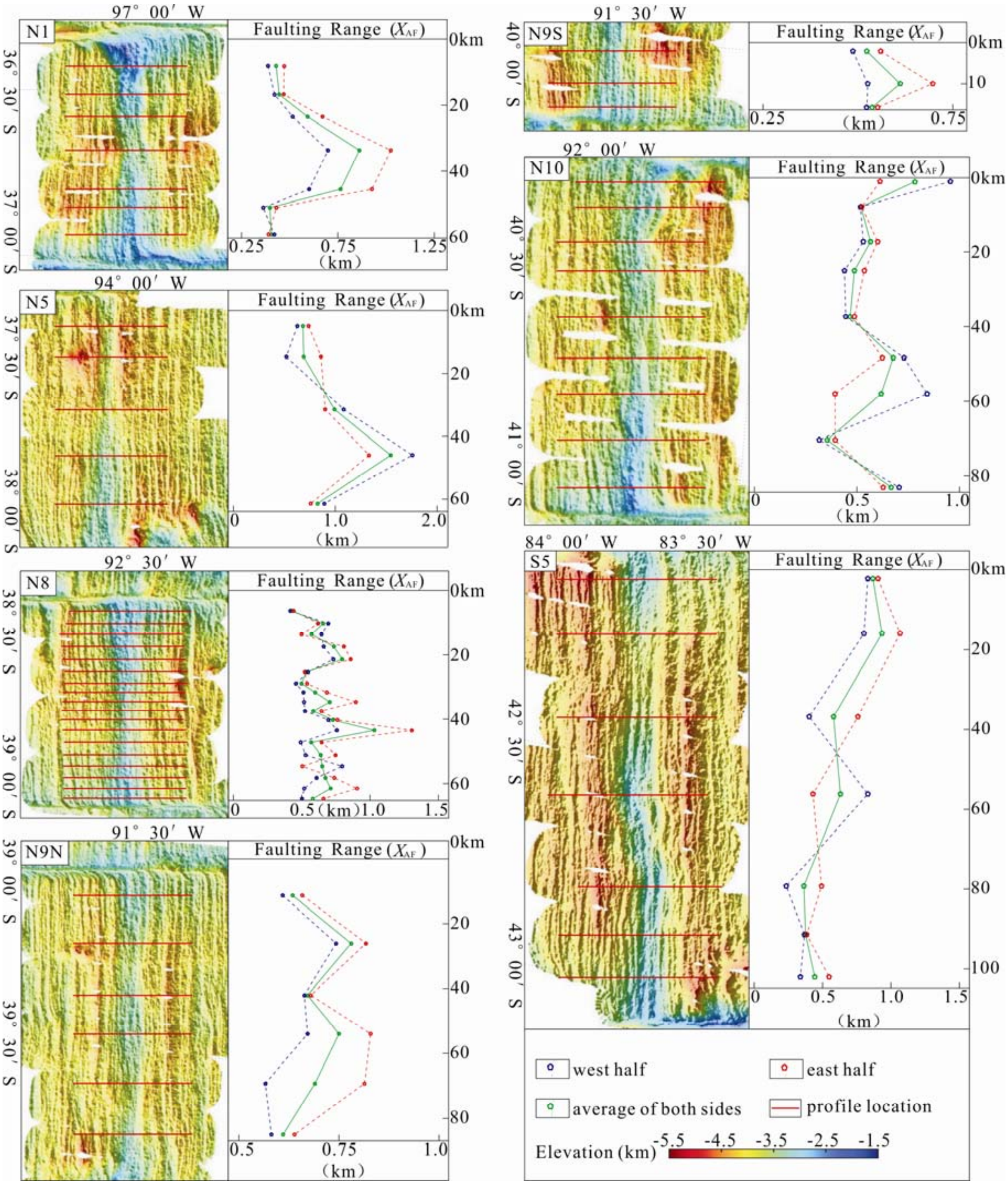

Fig. 8. Diagram showing the axial distribution of maximum migration distance of active faults (X_{AF}) in North Chile Rise
The first column is the bathymetry and location of topographic profiles, and the second is axial distribution of X_{AF}.

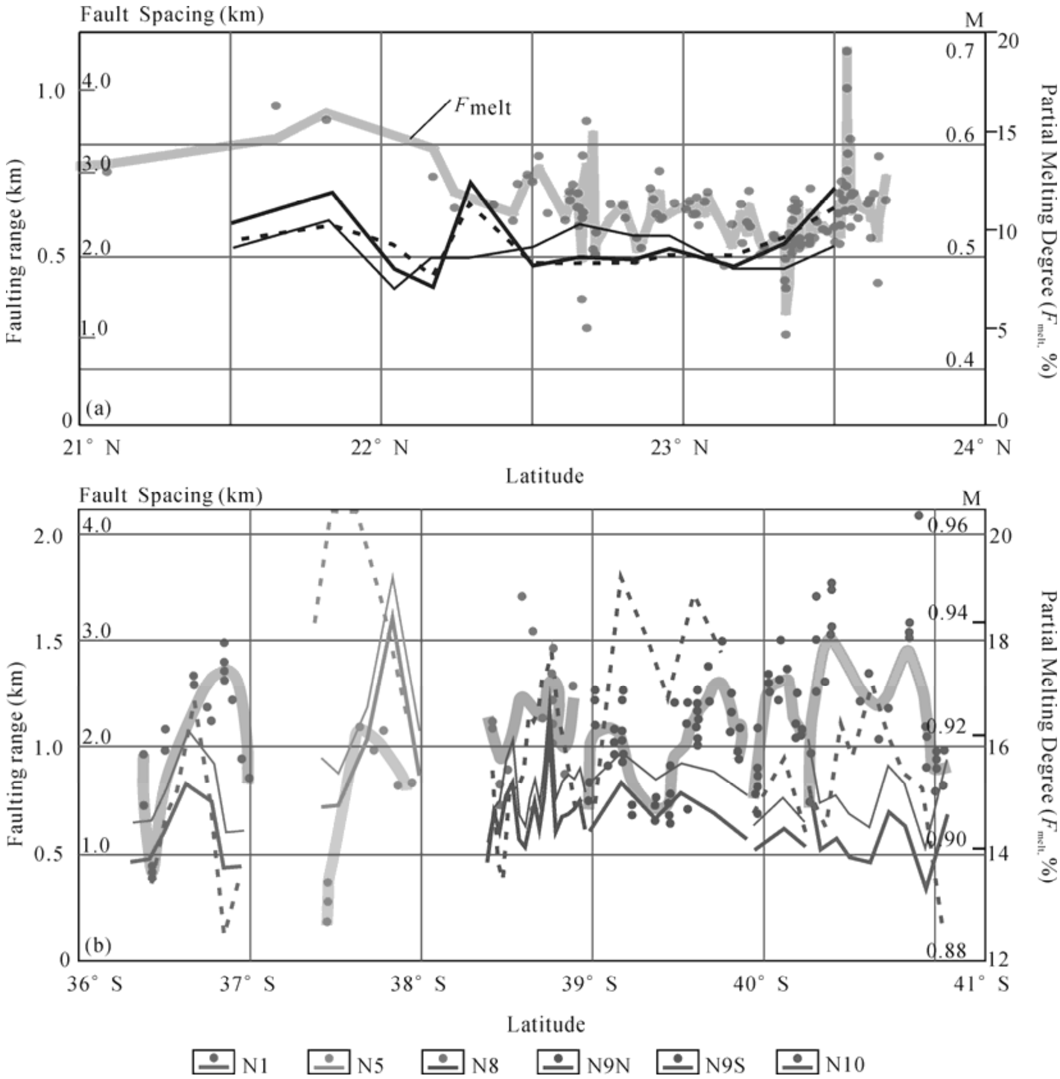

Fig. 9. Comparison of the faulting range on both halves of mid-ocean ridges

(a) Diagram showing the axial variations of X_{AF}, ΔS, partial melting degree (F_{melt}) and M in Mid–Atlantic Ridge 20° N–24° N (F_{melt} (%)=19.202-5.175Na$_8$+15.537Ca$_8$/Al$_8$, Niu and Batiza, 1991), the calculation of Na$_8$、Ca$_8$ and Al$_8$ is from Niu et al. (1996), and the geochemical data is from Pet DB; (b) diagram for axial variations of X_{AF}, ΔS, F_{melt} and M in North Chile Rise (Howell et al., 2016). In diagrams above, fine solid lines denote ΔS, medium solid lines denote average X_{AF} values, thick solid lines indicate the axial melting trend, and dashed lines mean M values.

ridge ends, M decreases and ΔS increases, resulting in a decrease of n values, but the weakening magmatism will lead to a colder and thicker lithosphere, which inversely causes ΔS to decrease and n to increase (Behn and Ito, 2008). The extent of the magma supply and the lithospheric thickness have completely inverse influence on the n value. To examine this, the two study areas can be divided into two endmembers. At the high-M NCR study area, the magma supply is sufficient in all ridge segments, and axial variation is nearly negligible, so there is a little direct impact on ΔS. The number of faults at this end member is directly affected by the axial variation of lithospheric thickness. Therefore, there is no correlation between n and M values, but there is a positive relationship between ΔS and M values (Fig. 9b). Therefore, a distinctly positive correlation between X_{AF} and M values is established (*Eq.*11). At the NMAR study area that has a relatively low partial melting fraction and an overall cold and thick lithosphere, the axial variation of M values becomes distinct. The number of faults (n) is affected by both the axial variation of the magma supply and the lithospheric thickness, thus making the positive correlation between the faulting range and partial melting degree of magma (or M values) less obvious than at the NCR (Fig. 9a). Here, it can be inferred that, at some ridge segments with extremely low supply of magma (i.e., ultraslow-spreading ridges), the positive correlation between X_{AF} and magma supply (M values) may disappear or even be replaced by an inverse relationship.

4.2 Advantages and limitations

The method for assessing active fault migration distance proposed here is easier and more economical than obtaining a faulting range from micro-seismic results

(Wolfe et al., 1995). However, there are some limitations in the multi-beam bathymetry method. First, the calculated X_{AF} values are not related to the median rift valley, so in order to predict the prepotent off-axis range of potential hydrothermal vents in mid-ocean ridges, the specific size of the median rift must be determined artificially. Secondly, X_{AF} values calculated through bathymetry data may be further diverged from reality in local areas than other methods. Finally, in view of its limitations, X_{AF} values can be used to predict the potential hydrothermal vents out of the median rift valley of mid-ocean ridges, which are mainly influenced by off-axial faulting (e.g., Lost City hydrothermal field, Kelly et. al., 2005), but cannot predict the hydrothermal activities in the median valley.

5 Conclusions

(1) Fault elements such as Fault Heave (ΔX) and Fault Spacing (ΔS) for both sides of mid-ocean ridges can be identified and quantitatively measured by Fourier filtering of seafloor multi-beam bathymetry in combination with the distribution pattern of the topographic slope, curvature, and slope direction. On the basis of the Sequential Faulting Model, Fault Heave and Fault Spacing can be used to assess the faulting range of both sides of mid-ocean ridges.

(2) Calculation results show that the distribution range of ΔS in NMAR 20°N–24°N is 2.92–3.79 km, and the distribution range of ΔX is 1.33–1.82 km. The range for X_{AF} is 0.76–1.01 km. These three axial distribution patterns are all characterized by "small in the center, large at both ends." In the NCR, the smallest X_{AF} is about 0.10 km, and the largest is up to 10.25 km. The axial distribution patterns of these segments include "small in the center part, large at both ends" (N9N, N10), "large in the center, small at both ends" (N1, N9S), "increasing from one end to the other" (N5, S5), and "zigzag" (N8).

(3) When the number of faults (n) for a specific distance is certain, the X_{AF} values on both sides of the mid-ocean ridges are proportional to the M values, and (n) is affected by factors such as lithospheric thickness, M values, and magmatic cycle.

(4) The faulting ranges in both study areas are positively related to the axial variation of magmatism. At the NCR study area, which has a sufficient magma supply, the fault number is mainly affected by the axial variation of lithospheric thickness, and there is a distinctly positive correlation between the faulting range and the axial variation of M values. At the NMAR study area, which has a relatively low partial melting degree, where fault number may be influenced by the axial variation of lithospheric thickness and M values, this positive relationship becomes less obvious.

Acknowledgments

This study was supported by the grant of China Ocean Mineral Resources R & D Association (DY135-S2-1-01; DY135-S1-1-03). We thank the reviewers and editors for their constructive feedback. This work greatly benefited from discussion with Jean-Arthur Olive.

Manuscript received Aug. 1, 2018
accepted Dec. 20, 2018
associate EIC YANG Jingsui
edited by LIU Lian

References

Behn, M.D., and Ito, G., 2008. Magmatic and tectonic extension at mid–ocean ridges: 1. Controls on fault characteristics. Geochemistry Geophysics Geosystems, 9(8): 4177–4183.

Buck, W.R., 1993. Effect of lithospheric thickness on the formation of high–and low–angle normal faults. Geology, 21 (10), 933.

Buck, W.R., Lavier, L.L., and Poliakov, A.N., 2005. Modes of faulting at mid–ocean ridges. Nature, 434(7034): 719.

Canales, J.P., Collins, J.A., and Escartín, J., 2000. Seismic structure across the rift valley of the Mid–Atlantic Ridge at 23°20′ (MARK area): Implications for crustal accretion processes at slow spreading ridges. Journal of Geophysical Research: Solid Earth, 105(B12): 28411–28425.

Chen, J., Tao, C., Liang, J., Liao, S., Dong, C., Li, H., Li, W., Wang, Y., Yue, X., and He, Y., 2018. Newly discovered hydrothermal fields along the ultraslow-spreading Southwest Indian Ridge around 63° E. Acta Oceanologica Sinica, 37(11): 61–67.

Corliss, J.B., Dymond, J., and Gordon, L.I., 1979. Submarine thermal springs on the Galápagos Rift. Science, 203(4385): 1073.

Escartín, J., Cowie, P.A., and Searle, R.C., 1999. Quantifying tectonic strain and magmatic accretion at a slow spreading ridge segment, Mid-Atlantic Ridge, 29°N. Journal of Geophysical Research, 1041(1041): 10421–10438.

Fan, Q., Li, J., Liu, C., and Pan, X., 2018. A study on the influence of oceanic core complex development on the migration of ridge axis. Acta Geologica Sinica, 92(10): 2040–2050 (in Chinese with English abstract).

Forsyth, D.W., 1992. Finite extension and low-angle normal faulting. Geology, 20(1): 27–30.

Franklin, J.M., Sangster, D.M., and Lydon, J.W., 1981. Volcanic –associated Massive Sulfide Deposits. In: Skinner, B.J., Economic Geology Seventy–fifth Anniversary Volume. Littleton: Society of Economic Geologists, 485–627.

German, C.R., and Parson, L.M., 1998. Distributions of hydrothermal activity along the Mid–Atlantic Ridge: interplay of magmatic and tectonic controls. Earth and Planetary Science Letters, 160(3–4): 327–341.

Goff, J.A., Tucholke, B.E., Lin, J., Jaroslow, G.E. and Kleinrock, M.C., 1995. Quantitative analysis of abyssal hills in the Atlantic Ocean: A correlation between inferred crustal thickness and extensional faulting. Journal of Geophysical Research: Solid Earth, 100(B11): 22509–22522.

Hannington, M., Jamieson, J., Monecke, T., Petersen, S., and Beaulieu, S., 2011. The abundance of seafloor massive sulfide deposits. Geology, 39(12): 1155–1158.

Herzig, P.M., and Hannington, M.D., 1995. Polymetallic massive sulfides at the modern seafloor a review. Ore Geology Reviews, 10(2): 95–115.

Howell, S.M., Ito, G., and Behn, M.D., 2016. Magmatic and tectonic extension at the Chile Ridge: Evidence for mantle controls on ridge segmentation. Geochemistry Geophysics Geosystems, 17(6): 2354–2373.

Kappel, E.S., and Franklin, J.M., 1989. Relationships between geologic development of ridge crests and sulfide deposits in the Northeast Pacific Ocean. Economic Geology, 84(3): 485–505.

Karson, J.A., and Rona, P.A., 1990. Block–tilting, transfer faults, and structural control of magmatic and hydrothermal processes in the TAG area, Mid–Atlantic Ridge 26°N. Geological Society of America Bulletin, 102(12): 1635–1645.

Kelley, D.S., Karson, J.A., Früh-Green, G.L., Yoerger, D.R., Shank, T.M., Butterfield, D.A., Hayes, J.M., Schrenk, M.O., Olson, E.J., Proskurowski, G., Jakuba, M., Bradley, A., Larson, B., Ludwig, K., Glickson, D., Buckman, K., Bradley, A.S., Brazelton, W.J., Roe, K., Elend, M.J., Delacour, A., Bernasconi, S.M., Lilley, M.D., Baross, J.A., Summons, R.E., and Sylva, S.P., 2005. A serpentinite-hosted ecosystem: the Lost City hydrothermal field. Science, 307(5714): 1428-1434.

Langmuir, C., Humphris, S., and Fornari, D., 1997. Hydrothermal vents near a mantle hot spot: the Lucky Strike vent field at 37° N on the Mid-Atlantic Ridge. Earth and Planetary Science Letters, 148(1–2): 69–91.

Larson, R.L., Searle, R.C., and Kleinrock, M.C., 1992. Roller–bearing tectonic evolution of the Juan Fernandez microplate. Nature, 356(6370): 571–576.

Lavier, L.L., Buck, W.R., and Poliakov, A.N.B., 2000. Factors controlling normal fault offset in an ideal brittle layer. Journal of Geophysical Research: Solid Earth, 105(B10): 23431–23442.

Liang, Y., Li, J., Li, S., Ni, J., and Ruan, A., 2014. The Magmato -tectonic dynamic model for the Indomed-Gallieni segment of the central southwest Indian ridge. Chinese Journal of Geophysics, 57(09): 257–269.

Liu, C., Li, J., Zhang, H., Liu, Z., and Fan, Q., 2018. Magma supply of the southwest Indian ocean: evidence from crustal thickness anomalies. Chinese Journal of Geophysics, 61(7): 2859–2870.

Liu, Z., and Buck, W.R., 2018. Magmatic controls on axial relief and faulting at mid-ocean ridges. Earth and Planetary Science Letters, 491(2018): 226–237.

Macdonald, K.C., 1982. Mid–ocean ridges: Fine scale tectonic, volcanic and hydrothermal processes within the plate boundary zone. Annual Review of Earth and Planetary Sciences, 10(1): 155–190.

Maia, M., and Gente, P., 1998. Three–dimensional gravity and bathymetry analysis of the Mid–Atlantic Ridge between 20°N and 24°N: Flow geometry and temporal evolution of the segmentation. Surface and Interface Analysis, 103(B1): 951–974.

Mcallister, E., and Cann, J.R., 1996. Initiation and evolution of boundary–wall faults along the Mid–Atlantic Ridge, 25–29° N. Geological Society of London, 118(1): 29–48.

Niu, Y., and Batiza, R., 1991. An empirical method for calculating melt compositions produced beneath mid-ocean ridges: Application for axis and off–axis (seamounts) melting. Journal of Geophysical Research: Solid Earth, 96(B13): 21753–21777.

Niu, Y., Waggoner, D.G., Sinton, J.M., and Mahoney, J.J., 1996. Mantle source heterogeneity and melting processes beneath seafloor spreading centers: The East Pacific Rise, 18°-19°S. Journal of Geophysical Research: Atmospheres, 1012(12): 27711–27734.

Olive, J.A., and Behn, M.D., 2014. Rapid rotation of normal faults due to flexural stresses: An explanation for the global distribution of normal fault dips. Journal of Geophysical Research: Solid Earth, 119(4): 3722–3739.

Olive, J.A., Behn, M.D., and Ito, G., 2015. Sensitivity of seafloor bathymetry to climate–driven fluctuations in mid-ocean ridge magma supply. Science, 350(6258): 310.

Pockalny, R.A., Smith, A., and Gente, P., 1995. Spatial and temporal variability of crustal magnetization of a slowly spreading ridge: Mid–Atlantic Ridge (20°–24° N). Marine Geophysical Research, 17(3): 301–320.

Rona, P.A., Klinkhammer, G., and Nelsen, T.A., 1986. Black smokers, massive sulphides and vent biota at the Mid-Atlantic Ridge. Nature, 321(6065): 33–37.

Ryan, W.B.F., Carbotte, S.M., and Coplan, J.O., 2009. Global multi–resolution topography synthesis. Geochemistry Geophysics Geosystems, 10(3): 395–397.

Searle, R.C., and Escartín, J., 2004. The rheology and morphology of oceanic lithosphere and mid–ocean ridges, in mid–ocean ridges: Hydrothermal interactions between the lithosphere and oceans. In: Washington DC American Geophysical Union Geophysical Monograph Series, 148: 63–93.

Shaw, P.R., and Lin, J., 1993. Causes and consequences of variations in faulting style at the Mid–Atlantic Ridge. Journal of Geophysical Research: Solid Earth, 98(B12): 21839–21851.

Small, C., 1994. A global analysis of mid–ocean ridge axial topography. Geophysical Journal International, 116(1): 64–84.

Small, C., 1998. Global systematics of mid-ocean ridge morphology. In: Washington DC American Geophysical Union Geophysical Monograph Series, 106: 1–25.

Smith, D., 2013. Tectonics: Mantle spread across the sea floor. Nature Geoscience, 6(4): 247–248.

Stoddard, P.R., and Jurdy, D.M., 2012. Topographic comparisons of uplift features on Venus and Earth: Implications for Venus tectonics. Icarus, 217(2): 524–533.

Tao, C., Li, H., Huang, W., Han, X., Wu, G., Su, X., Zhou, N., Lin, J., He, Y., and Zhou, J., 2011. Mineralogical and geochemical features of sulfide chimneys from the 49°39′E hydrothermal field on the Southwest Indian Ridge and their geological inferences. Chinese Science Bulletin, 56(26): 2828.

Tao, C., Lin, J., and Guo, S., 2012. First active hydrothermal vents on an ultraslow–spreading center: Southwest Indian Ridge. Geology, 40(1): 47–50.

Tebbens, S.F., Ce, S.C., and Kovacs, L., 1997. The Chile ridge: A tectonic framework. Journal of Geophysical Research, 102 (6): 12035–12059.

Wolfe, C.J., Purdy, G.M., and Toomey, D.R., 1995. Microearthquake characteristics and crustal velocity structure at 29° N on the Mid–Atlantic Ridge: The architecture of a slow spreading segment. Journal of Geophysical Research: Atmospheres, 100(B12): 24449–24472.

Yu, Z., Li, J., Liang, Y., Han, X., Zhang, J., and Zhu, L., 2013. Distribution of large-scale detachment faults on mid-ocean ridges in relation to spreading rates. Acta Oceanologica Sinica, 32(12): 109–117.

About the First Author

FAN Qingkai, male, born in 1991, Ph. D. candidate, now majoring in geology in the School of Earth and Space Science, Peking University, mainly engaged in structural geology and hydrothermal mineralization in mid-ocean ridges. E-mail: 18810812308@163.com

About the Corresponding Author

LI Jianghai, male, born in 1965, Ph. D., professor of School of Earth and Space Science, Peking University, mainly engaged in global tectonics and mid-ocean ridges. E-mail: jhli@pku.edu.cn